



Effects of Ti content on the tensile ductility, lattice distortion and mechanical properties of VN_xTaTi_x refractory high-entropy alloys

Lingjie Yang ^{a,1}, Kai Xiong ^{a,b,*¹}, Chengchen Jin ^a, Hua Dai ^c, Haijun Wu ^{c,**}, Shunmeng Zhang ^a, Junjie He ^a, Yingwu Wang ^{d,***}, Yong Mao ^a

^a Materials Genome Institute, National Center for International Research on Photoelectric and Energy Materials, School of Materials and Energy, Yunnan University, Kunming, 650091, China

^b Department of Physics, Tsinghua University, Beijing, 100084, China

^c Kunming Institute of Precious Metals, Yunnan Precious Metals Laboratory Co., Ltd, Kunming, 650106, China

^d School of Engineering, Yunnan University, Kunming, 650091, China



ARTICLE INFO

Keywords:

Refractory high-entropy alloys
Mechanical properties
Lattice distortion
Dislocation
Kink bands

ABSTRACT

Refractory high-entropy alloys (RHEAs) have remarkable properties like high strength and thermal stability at high temperatures. Their practical application is hindered by ambient brittleness and inferior formability. Titanium (Ti) is recognized as a crucial element in improving the ductility and oxidation resistance of RHEAs, but its plasticizing mechanism is still unclear. To address this, a series of body-centered cubic (BCC) single-phase VN_xTaTi_x alloys were designed. The alloys exhibited exceptional ductility and cold-rolling formability at room temperature. Remarkably, the tensile fracture elongation of VN_xTaTi_x alloy was about 26.9%, which surpassed most RHEAs. The major plastic mechanisms of the alloys are $a/2<1\ 1 1>$ -type dislocation and $\{1\ 1 2\}<1\ 1 1>$ -type twinning. Solid solution strengthening was identified as the primary strengthening mechanism. Although Ti reduced the solid solution strengthening effect, it contributed to weight reduction and enhanced local lattice distortion. This study not only designed several RHEAs with ductility but also provided insights into the effect of Ti content on their phase stability, lattice distortion, and strength mechanisms. These findings have significant implications for designing new RHEAs with ambient ductility.

1. Introduction

Refractory high-entropy alloys (RHEAs) have attracted extensive attention due to their exceptional high-temperature strength, superior irradiation resistance, and remarkable stability under elevated temperatures [1]. These alloys hold great promise as structural materials for high-temperature applications in aerospace, petroleum, and nuclear industries [2]. Most of RHEAs are primarily composed of refractory elements from IVB to VIB groups in the periodic table [2]. In comparison to conventional refractory metals, RHEAs exhibit high strength and softening resistance at elevated temperature. For instance, the compressive yield strength of NbMoTaW alloy is 1058 MPa at room temperature (RT), which remains at 405 MPa even at 1600 °C [3].

Similarly, the NbMoTaWV alloy exhibits a compressive yield strength of 1246 MPa at RT and 477 MPa at 1600 °C, surpassing most of commercial high-temperature alloys, e.g. Inconel 718 and Haynes 230 superalloys [3]. CrMoNiV alloy exhibits high compressive yield strength of 1518 MPa at RT and maintains 1000 MPa at 1273 K [4]. However, most RHEAs tend to be brittle at room temperature (RT), hindering their industrial applications. For example, the compressive fracture strain of NbMoTaW and NbMoTaWV alloys is only 2.6% and 1.7% at RT, respectively [3]. The compressive fracture strain of the CrMoNiV alloy is also less than 5% [4]. The brittleness of RHEAs makes them susceptible to crack during cold working, thus their plastic forming is challenging at RT. The plastic forming of brittle RHEAs has to be performed at high temperature. Nevertheless, hot working is accompanied by challenges in

* Corresponding author. Materials Genome Institute, National Center for International Research on Photoelectric and Energy Materials, School of Materials and Energy, Yunnan University, Kunming, 650091, China.

** Corresponding author.

*** Corresponding author.

E-mail addresses: xiongkai@ynu.edu.cn (K. Xiong), whj@ipm.com.cn (H. Wu), 370076779@ynu.edu.cn (Y. Wang).

¹ L. Yang and K. Xiong contributed equally to this work.

metallic oxidation and higher energy consumption. Consequently, the development of new RHEAs with both high strength and good ductility has emerged as a research forefront in the field of metallic materials.

Several ductile RHEAs systems have been developed by substituting elements Cr, Mo, Ta, and W with Ti, Zr, Hf, V and Nb. For instance, the HfNbTaTiZr alloy exhibits high strength and good ductility at RT, maintaining a single-phase BCC structure over a wide temperature range [5]. The TiHfVNbTa alloy demonstrates excellent ambient ductility and cold-rolling formability, with a rolling deformation >84% and a tensile yield strength of up to 1340 MPa, surpassing most of RHEAs [6]. The TiVNbHf alloy exhibits tensile yield strength about 1004 MPa and fracture elongation 16.1% [7]. The newly developed Al_{0.5}Ti₂Nb₁Zr₁W_{0.5} alloy exhibits excellent compressive plasticity (>68%) at 298 K [8]. The lightweight AlTiVCoNi alloy displays an exceptional compressive yield strength about 1631 MPa at 20 °C [9]. The ductile (TiNbZr)₈₉(AlTa)₁₁ alloy has a low density of 6.0 g cm⁻³ and excellent compressive plasticity of ~70% at 298 K [10]. The at-cast Hf₁₅Nb₄₀Ta₂₅Ti₁₅Zr₅ alloy can be cold-rolled to a thickness reduction of >90% at RT without intermediate annealing [11]. The VNbTa alloy demonstrates exceptional combined properties of tensile yield strength (1033 MPa), outstanding fracture elongation (>19%) and excellent rolling formability (>80% thickness reduction) at RT, surpassing most of traditional RMEAs [12, 13]. Adjusting the Ti/V ratio can enhance the ductility of the alloys, e.g., the fracture elongation of Ti₃₈V₁₅Nb₂₃Hf₂₄ alloy increases to 20.6%, but the yield strength decreases to 774 MPa [7]. Adjusting the Ti/Ta ratio in TiZrNbTa alloy induces a brittle-to-ductile transition, i.e., the fracture elongation increased from 5% (TiZrNbTa) to 22% (Ti₄₅Zr₂₅Nb₂₅Ta₅) [7]. Increasing the Ti content also benefits to improve the ductility of TiZrNbVAL alloy, e.g. the fracture elongation of Ti₅₀Zr₁₈Nb₁₅V₁₂Al₅ alloy reaches to 47% [14]. Ti addition enhances both the ductility and strength of NbMoTaW alloy, i.e., the compressive fracture strain increases from 1.9% (NbMoTaW) to 11.5% (TiNbMoTaW), and the compressive yield strength increases from 996 MPa (NbMoTaW) to 1455 MPa (TiNbMoTaW) [15]. Adding an appropriate amount of Ti to (HfNbTa)_{1-x}Ti_x alloys can reduce their density and Young's modulus, and enhance their ductility and cold-rolling formability at RT [16]. The addition of Ti can improve the corrosion resistance of RHEAs as well [17]. These studies reveal that Ti is one of key elements for enhancing the ductility of RHEAs, but the physical mechanisms of ductility improvement are still not well understood and require additional exploration.

Transmission electron microscopy (TEM) observations have confirmed that the ductile deformation of RHEAs is primarily associated with the motion of dislocations, the formation of kink bands, and the occurrence of twins [18–21]. Molecular dynamics (MD) simulations have indicated that the excellent ductility of Ti-containing RHEAs is mainly attributed to the motion of *a*/2<1 1 2>-type dislocations [16]. The increase of Ti content can reduce the shear modulus of RHEAs [16], which is beneficial to lower the critical shear stress required for dislocation generation and movement, ultimately enhancing the ductility of RHEAs [22]. Additionally, density functional theory (DFT) calculations have demonstrated that the increase of Ti content in RHEAs can exacerbate local lattice distortion [16]. The local lattice distortion is closely related to the asymmetric charge distribution induced by multiple elements in RHEAs [16]. Lattice distortion, as one of the “four core effects” of high-entropy alloys, plays a crucial role in keeping their phase stability and maintaining high strength [1]. Local lattice distortion creates a non-uniform stress field within the alloys, which can hinder the motion of dislocations and helps to slow down the strength loss [14]. Currently, research on the influence of Ti on the lattice distortion, strengthening and plastic mechanisms of RHEAs is still in its initial stage, more in-depth works need to be performed.

The main objective of this study is to investigate the influence of Ti content on the phase stability, structural and mechanical properties of RHEAs. To achieve this, a series of new VNbTaTi_x ($x = 0.0, 0.5, 1.0, 1.5$) alloys were designed. Thermochemical empirical parameters, phase

diagram calculations, X-ray diffraction (XRD) and scanning electron microscopy (SEM) observations were employed to analyze the effect of Ti content on the phase stability of the alloys. Tensile testing, hardness measurements and strengthening theory analysis were combined to explore the impact of Ti content on their yield strength and ductility. Cold rolling, electron backscatter diffraction (EBSD) and MD simulations were utilized to investigate their plastic deformation mechanisms, particularly the mechanisms related to dislocation nucleation, kink bands and twins formation. The lattice distortion of the alloys was quantitatively analyzed by combining density functional theory (DFT) calculations and MD simulations.

2. Methods

2.1. Experimental procedures

VNbTaTi_x ($x = 0.0, 0.5, 1.0, 1.5$) alloy ingots were prepared from the raw materials of high-purity metals Ti (99.95 wt%), V (99.95 wt%), Nb (99.95 wt%), and Ta (99.95 wt%) by using a vacuum arc melting furnace (HVAM-B, China) in a high-purity argon atmosphere (>99.95%) under an operating current of 400 A. The ingots were flipped and remelted more than 6 times to ensure homogenous composition. The as-cast ingots were about 25 mm in diameter and about 7 mm in thickness with a mass of ~37 g. The ingots were rolled into sheets at a rolling speed 150 mm s⁻¹ using a double-high rolling mill (JH-RZH-110, China) without lubrication. The final thickness of the sheets was about 1.4 mm corresponding to over 80% thickness reduction. Several dog-bone shaped tension samples with a 16 mm in gage length, 12 mm in width and 1 mm in thickness were tailored from the rolled sheets along the rolling direction using an electrical discharge machining (DK77, China). The dog-bone samples were sealed in a quartz tube with 0.005 torr vacuum, annealed at 1200 °C 45 min and immediately followed by water quenching to get recrystallized microstructure. The tension tests of the annealed samples were conducted using an electronic universal testing machine (ETM205D, China) with a constant strain rate 0.001 s⁻¹ at RT. Microhardness (HV) was tested using a Vickers MHV-1000 hardness tester.

In order to detect the phase composition of the alloys, XRD analysis was conducted using an X-ray diffractometer (Rigaku Smartlab SE, Japan) with Cu-K α radiation ($\lambda = 0.15406$ nm) and 2 θ angle range from 20° to 90°. Metallographic specimens were grinded successively from 300 grit to 3000 grit waterproof abrasive papers, and then polished with W2.5 polishing pastes (2 μ m in particle size). The microstructure of the alloys was observed by using a field emission SEM (Tescan Amber, Czech) at 20 KV voltage and 10 nA current in the secondary-electron and backscattered-electron (BSE) modes. The chemical compositions of the alloys were detected by the energy-dispersive X-ray spectroscopy (EDS) (Oxford Ultim Max 40, UK). Back-scattering diffraction measurements were performed by using an EBSD camera (Oxford Symmetry, UK) at a scanning step of 0.4 μ m. The EBSD samples were polished in an HClO₄: CH₃OH (1:9) electrolyte at 20 V about 40 s. The mass density of the alloys was measured by the Archimedes drainage method according to the ASTM B962-17 international standard.

2.2. Computational methods

Multiple computational methods (CALPHAD, MD and DFT) were combined to investigate the effect of Ti content on the phase formation, mechanical and physical properties of VNbTaTi_x alloys. CALPHAD calculations were carried out using the TCHEA5 database of the commercial Thermo-Calc software to predict the equilibrium phases of VNbTaTi_x alloys. MD simulations were performed to analyze the effect of Ti content on the tensile properties of VNbTaTi_x alloys. The periodic simulation boxes for tension were about 30 nm × 30 nm × 30 nm in sizes and $\mathbf{x} = [1 \ 1 \ 1]$, $\mathbf{y} = [1 \bar{1} \ 0]$, and $\mathbf{z} = [1 \ 1 \ \bar{2}]$ in orientations, containing

more than 1.41 million atoms in each box. Elements were randomly occupied the BCC lattice sites in simulations box (Fig. S1 in Supplements). The simulation boxes were uniformly stretched along the x direction with a constant strain rate 10^9 s^{-1} . In addition, a periodic simulation box containing 10 nanograins was applied to perform compression simulation of VNbTaTi polycrystal to discuss the role of grain boundaries in compressive deformation. The simulation box was about $30 \text{ nm} \times 30 \text{ nm} \times 30 \text{ nm}$ in sizes, including more than 1.58 million atoms. Elements were also randomly located the BCC lattice sites of the nanograins (Fig. S2 in Supplements). The average size of the nanograins was about 13.7 nm. Before deformation, all simulation boxes were fully relaxed ($>50 \text{ ps}$) at 300 K temperature and zero pressure by the Nose-Hoover thermostat within an isobaric-isothermal (NPT) ensemble [23]. All MD simulations were carried out with an open-source LAMMPS code [24]. The time step of MD simulations was 1.0 fs. The interatomic force and energy of V-Nb-Ta-Ti systems were computed using a recently developed interatomic potential [25]. All atomistic configurations were visualized by OVITO software [26].

DFT calculations were performed to investigate the effect of Ti content on the lattice distortion and electronic properties of VNbTaTi_x alloys. A special-quasirandom-structures (SQS) method was utilized to construct random supercells for these alloys [27]. The SQS method incorporates a Monte Carlo optimization algorithm to ensure the stochastic occupation of elements within the supercells [27]. The SQS method has been extensively utilized in the construction of supercells for high-entropy materials [28,29]. For each alloy composition, a systematic search was conducted to identify random supercells with a high degree of disorder, followed by structural optimization. During the optimization process, both atomic positions and supercell shapes were allowed to change, enabling the identification of energetically favorable supercells. Typical SQS supercells of VNbTaTi_x alloys were displayed in Fig. S3 (in Supplements). These optimized supercells were then utilized to calculate the elastic properties and electronic structures. The elastic properties are determined using the finite strain method, where seven strains ($\epsilon = 0.000, \pm 0.005, \pm 0.010, \pm 0.015$) are systematically applied along each crystallographic symmetry direction to obtain the stress-strain (σ - ϵ) relationship. Subsequently, the elastic constant matrix C , was derived based on the generalized Hooke's law ($\sigma = C\epsilon$). The electron localization function (ELF) and chemical bonding analyses were conducted to investigate the electronic structure and lattice distortion of the alloys. All DFT calculations were carried out by the VASP code [30]. The ion-electron interaction potential was described using the projector augmented wave (PAW) pseudopotential [31], while the exchange-correlation energy was approximated using the generalized gradient approximation (GGA-PBE) [32]. The plane wave cutoff energy was set at 600 eV. A Monkhorst-Pack $3 \times 3 \times 3$ k-point grid is employed to sample the first Brillouin zone. The convergence criteria for energy and forces were set to 10^{-6} eV and 0.01 eV \AA^{-1} , respectively.

3. Results and discussion

3.1. Phase formation and microstructure

The potential formation of phases in VNbTaTi_x alloys was predicted using classic thermodynamic parameters and CALPHAD calculations. The actual phases formed in non-equilibrium solidification were detected by XRD tests. Several thermodynamic parameters were utilized to predict the ability of multicomponent alloys to form single-phase solutions, including mixing enthalpy (ΔH_{mix}), mixed entropy (ΔS_{mix}), valence electron concentration (VEC), atomic size difference (δ), and Ω parameters [33,34].

$$\Delta S_{\text{mix}} = -R \sum_{i=1}^n c_i \ln c_i \quad (1)$$

$$\Delta H_{\text{mix}} = \sum_{i=1, i < j}^n 4c_i c_j H_{ij}^{\text{mix}} \quad (2)$$

$$\Omega = \frac{T_m \Delta S_{\text{mix}}}{|\Delta H_{\text{mix}}|} \quad (3)$$

$$\delta = \sqrt{\sum_{i=1}^n c_i \left(\frac{r_i - \bar{r}}{\bar{r}} \right)^2} \quad (4)$$

$$VEC = \sum_{i=1}^n c_i VEC_i \quad (5)$$

where R is the gas constant; n is the element types; c_i is the atomic concentration of the i-th element; H_{ij}^{mix} is the mixing enthalpy for the binary i-th and j-th elements; T_m is the average melting point of constituent elements; r_i is the atomic radius of the i-th element; \bar{r} is the average atomic radius; VEC_i is the valence electron concentration of the i-th element. The applied values of corresponding parameters are listed in Table S1 in Supplements. The criteria commonly accepted for determining whether an alloy is in a single-phase solid solution are as follows: $-22 \leq \Delta H_{\text{mix}} \leq 7 \text{ kJ mol}^{-1}$, $11 \leq \Delta S_{\text{mix}} \leq 19.5 \text{ J mol}^{-1}$, $\delta \leq 6.6\%$, and $\Omega \geq 1.1$ [33,34]. According to the values presented in Table 1, the ΔH_{mix} , ΔS_{mix} , δ , and Ω values of VNbTaTi_x alloys meet the empirical criteria, indicating the potential formation of single-phase solid solutions in these alloys. Additionally, an alloy tends to form a BCC single-phase solid solution when its valence electron concentration (VEC) is low (<6.87) [33]. The VEC values of VNbTaTi_x alloys fall within the range of 4.67–5.00, suggesting a high likelihood of BCC solid solution formation in these alloys.

Fig. 1 plots the calculated phase fraction as a function of temperature for equilibrium solidification of VNbTaTi_x alloys. In Fig. 1a, it can be observed that the Ti_{0.0} alloy undergoes solidification from a BCC single-phase solid solution as the temperature (T) decreases from 2391 °C to 2145 °C. There is a wider BCC single phase region in the range of 2145 °C–318 °C. Below 318 °C, a portion of BCC phase transforms into C15_Laves phase. Comparing Fig. 1a with Fig. 1b ~ c, it is seen that Ti addition results in decreasing the solidus temperature (T_s) from 2145 °C (Ti_{0.0} alloy) to 1886 °C (Ti_{1.5} alloy) and increasing the transformation temperature (T_t) from 318 °C (Ti_{0.0} alloy) to 436 °C (Ti_{1.5} alloy). This phenomenon suggests that the single-phase region becomes narrower with an increase in Ti content. Additionally, Ti addition promotes the precipitation of HCP_A3 phase (Fig. 1b). The precipitation temperature of HCP_A3 phase increases with increasing Ti content, while the precipitation temperature of C15_Laves phase is almost unaffected. The empirical criterion $(T_s - T_t)/T_s > 0.3$ is usually used to predict whether a single-phase solid solution formed during non-equilibrium solidification [16]. The calculated $(T_s - T_t)/T_s$ values are approximately 0.76, 0.72, 0.69, and 0.67 for the Ti_{0.0}, Ti_{0.5}, Ti_{1.0}, and Ti_{1.5} alloys, respectively. This result indicates that these alloys are likely to solidify into single-phase solid solutions during the smelting process.

Fig. 2a plots the XRD patterns of the as-cast VNbTaTi_x alloys, revealing a BCC single-phase structure. The diffraction angle (2θ) of the main peak shifts towards the left as the Ti content increases (as shown in the enlarged view on the right of Fig. 2a). The left shift indicates an increase in the lattice parameter of the alloys. To confirm this inference,

Table 1

The mixing enthalpy (ΔH_{mix}), mixed entropy (ΔS_{mix}), valence electron concentration (VEC), parameters δ and Ω of VNbTaTi_x alloys.

Alloys	ΔH_{mix} (kJ·mol ⁻¹)	ΔS_{mix} (J/K ⁻¹ ·mol ⁻¹)	δ	Ω	VEC
Ti _{0.0}	-0.889	9.131	0.040	28.00	5.00
Ti _{0.5}	-0.490	11.235	0.039	61.48	4.86
Ti _{1.0}	-0.250	11.522	0.037	116.6	4.75
Ti _{1.5}	-0.099	11.378	0.036	287.5	4.67

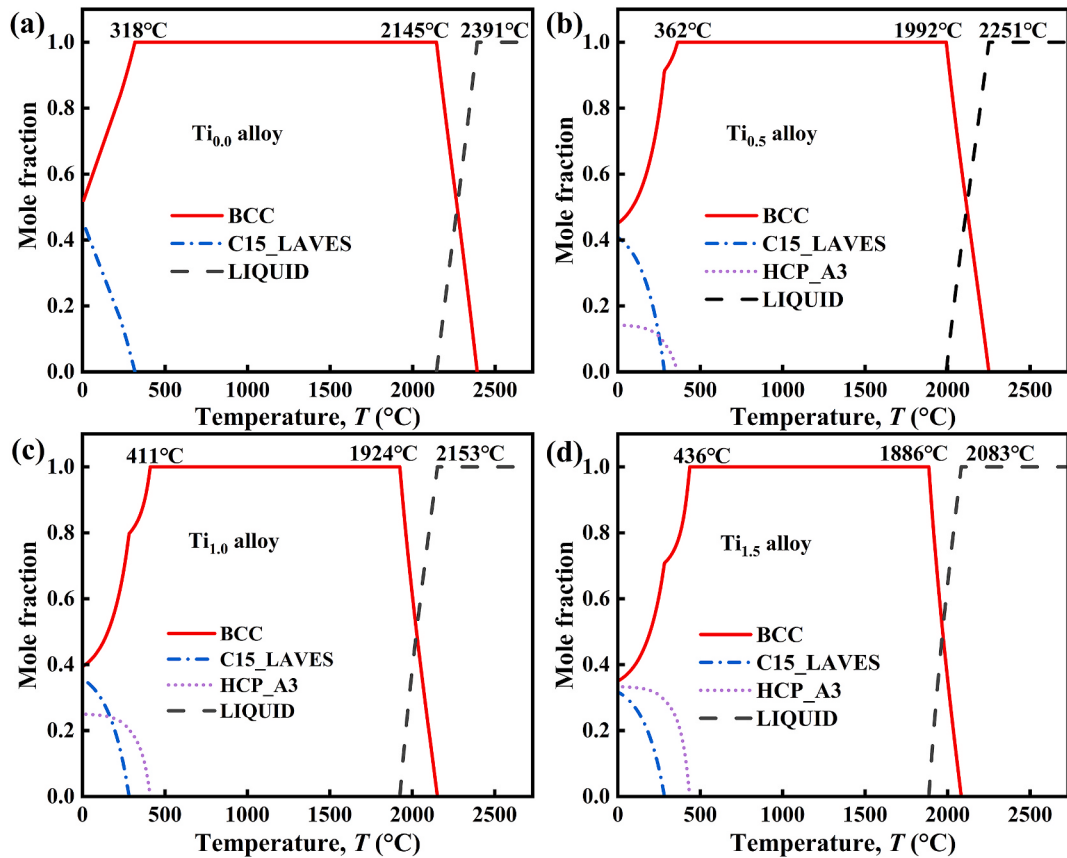


Fig. 1. Calculated phase fraction as a function of temperature for equilibrium solidification of VNbTaTi_x ($x = 0.0, 0.5, 1.0, 1.5$) alloys.

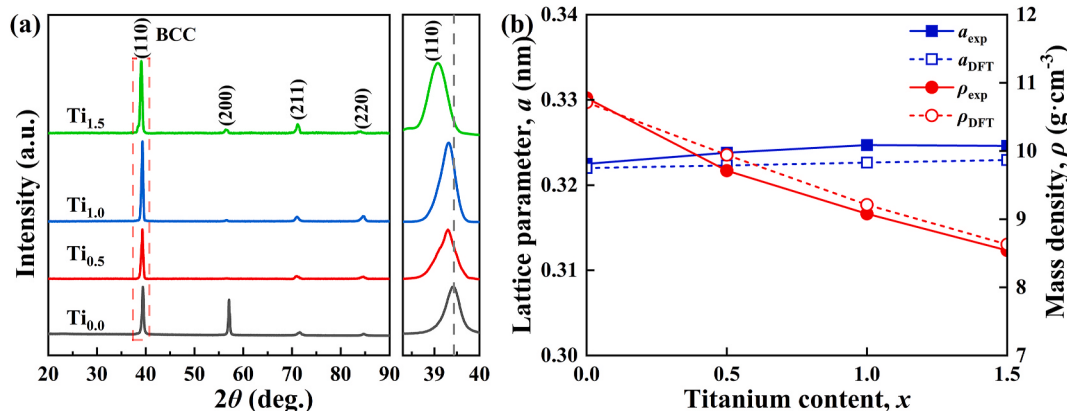


Fig. 2. (a) X-ray diffraction patterns of VNbTaTi_x ($x = 0.0, 0.5, 1.0, 1.5$) alloys. (b) Lattice parameter and mass density as a function of Ti content. The solid and dash curves are from XRD experiments and DFT calculations, respectively.

the lattice parameter of the alloys was calculated from the XRD patterns using the Bragg diffraction condition and compared with the results from DFT calculations. As shown in Fig. 2b, both the XRD tests and DFT calculations confirm that the lattice parameter of the alloys increases with increasing Ti content. Additionally, the mass density decreases from 10.07 ± 0.03 g cm⁻³ (Ti_{0.0} alloy) to 8.54 ± 0.02 g cm⁻³ (Ti_{1.5} alloy), suggesting that the addition of Ti helps to reduce the weight of RHEAs.

Fig. 3 displays the microstructure features and composition profiles of as-cast VNbTaTi_x alloys. The secondary electron images and BSE images reveal a typical dendritic microstructure, with no second phase is observed. As listed in Table 2, the measured chemical compositions of the alloys are close to their nominal compositions. The EDS mapping

images in Fig. 3 show significant micro-compositional segregation in the alloys. The high melting point Ta element tends to aggregate in dendritic regions, while the low melting point Ti and V elements enrich in interdendritic regions. The distribution of the Nb element is relatively homogeneous. This compositional segregation pattern is consistent with that observed in other RHEAs [6]. To quantitatively evaluate the extent of segregation for each element, a segregation ratio (k) is defined as $k = C_{DR}/C_{IR}$, where C_{DR} and C_{IR} are the elemental compositions in the dendritic and interdendritic regions, respectively [6]. The deviation of k values from 1 indicates the level of elemental segregation. The $k = 1$ denotes a uniform elemental distribution, $k > 1$ indicates that elements tend to aggregate in the dendritic regions, and $k < 1$ implies interdendritic segregation [35]. Fig. 4 shows that the high melting point Ta and

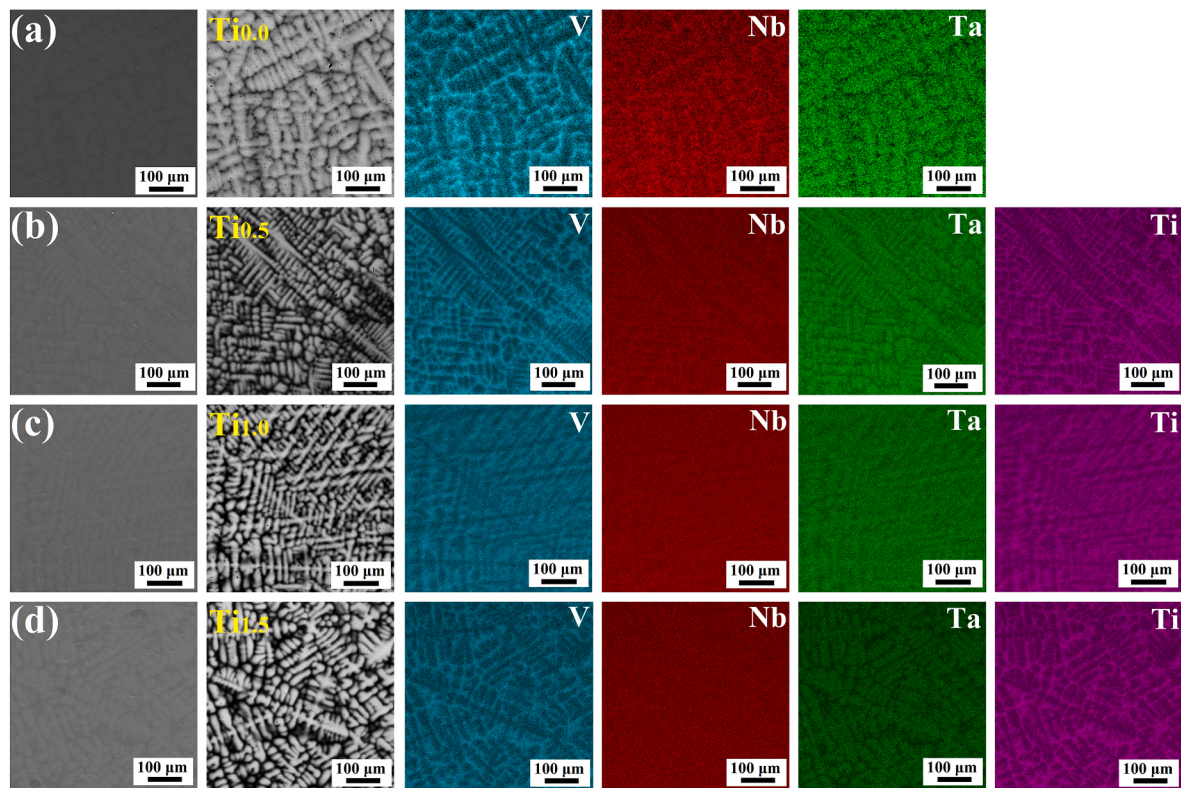


Fig. 3. The secondary electron images (the 1st column), backscattered electron (BSE) images (the 2nd column) and energy dispersive X-ray spectroscopy (EDS) mappings (the 3rd~6th columns) of as-cast VNbTaTi_x ($x = 0.0, 0.5, 1.0, 1.5$) alloys.

Table 2
SEM-EDS measured composition of as-cast VNbTaTi_x ($x = 0.0, 0.5, 1.0, 1.5$) alloys.

Alloys	Ti (at.%)	V (at.%)	Nb (at.%)	Ta (at.%)
Ti _{0.0}	—	37.0	35.1	27.9
Ti _{0.5}	14.2	27.7	27.8	30.3
Ti _{1.0}	25.2	25.0	24.1	25.7
Ti _{1.5}	33.4	23.2	22.1	21.2

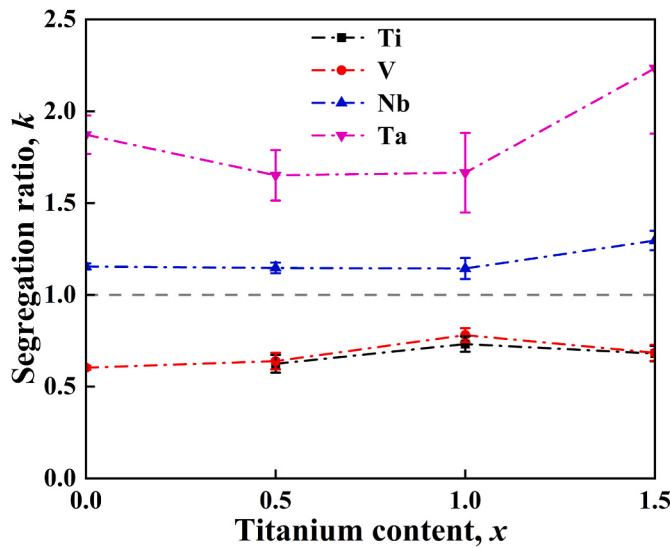


Fig. 4. Segregation ratio k of VNbTaTi_x ($x = 0.0, 0.5, 1.0, 1.5$) alloys.

Nb elements tend to aggregate in dendritic regions, while the low melting point Ti and V elements accumulate in interdendritic regions.

3.2. Microstructure of the cold-rolled sheets

Fig. 5 presents the XRD patterns of the VNbTaTi alloy under different cold-rolled states. As shown in **Fig. 5**, the number and location of XRD peaks are not significantly affected by cold rolling. This indicates that the BCC phase is stable, and no obvious solid-state phase transition occurs during the rolling process. The magnified view on the right of **Fig. 5** reveals that the (1 1 0) peak shifts to a smaller angle, suggesting an increase in the lattice parameter due to the effect of residual stress induced by rolling. Furthermore, the main peak gradually changes from (1 1 0) peak to (2 0 0) peak, indicating the formation of a deformation

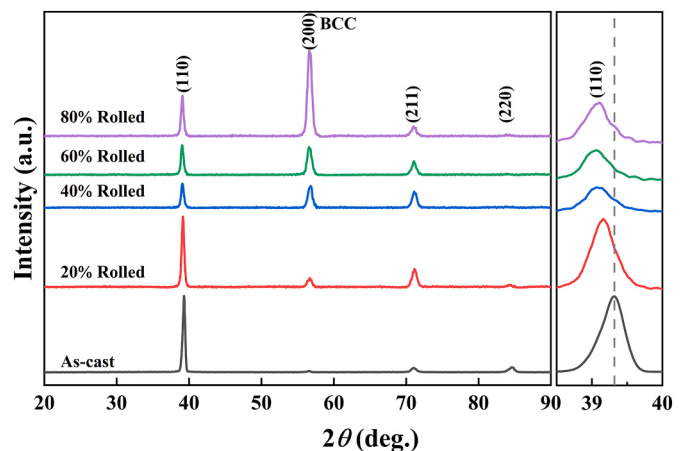


Fig. 5. X-ray diffraction patterns of TiVNbTa alloy under different rolling states.

texture during the rolling process [6].

Fig. 6 depicts the microstructure evolution of TiVNbTa alloy under different rolled conditions. The band contrast (BC) images in **Fig. 6a–e** demonstrate the expansion of plastic deformation regions (represented by black areas) with increasing rolling deformation. The inverse pole figure (IPF) maps in **Fig. 6f–j** provide compelling evidence of grain elongation along the rolling direction, leading to deformation texture and grain fragmentation in regions of high dislocation density (black areas). The Kernel average misorientation (KAM) maps in **Fig. 6k–o** reveal a significant rise in KAM values with increasing rolling deformation, indicating a simultaneous increase in dislocation density.

3.3. Kink band and mechanical twin formation

Fig. 7 presents the EBSD images of the 5% RIT and 20% RIT VNbTaTi samples. **Fig. 7a** shows the BC images of the 5% RIT sample, where the red regions highlight local crystal misorientation $>50^\circ$. The IPF image in **Fig. 7b** reveals the presence of numerous linear bands within the grains, exhibiting large misorientation. Notably, the local plastic strain around these linear bands and grain boundaries is noticeably higher compared to other regions (**Fig. 7c**). To quantitatively assess the misorientation between the linear bands and the matrix, a misorientation profile was plotted in **Fig. 7d** along the arrow in **Fig. 7b**. **Fig. 7d** indicates a misorientation angle of approximately 60° between the red linear regions and the matrix. Note that the misorientation aligns with the expected misorientation angle ($\sim 60^\circ$) observed in the $\{1\ 1\ 2\} <1\ 1\ 1>$ twin system of BCC metals. Additionally, **Fig. 7c** exhibits the $\{1\ 1\ 1\}$ and $\{1\ 1\ 2\}$ pole figures. It is evident from the $\{1\ 1\ 2\}$ pole figure that three overlapping points exist between the matrix (red points) and the bands (blue points), indicating a mirror symmetry relationship regarding the $\{1\ 1\ 2\}$ crystal planes. Moreover, the $\{1\ 1\ 1\}$ pole figure reveals one overlapping point, signifying that $<1\ 1\ 1>$ orientation serves as the

common symmetric rotation axis for both the matrix and the bands. The lattice rotation angle measures approximately 58° that is very close to the expected 60° . These findings confirm that the red linear bands belong to $\{1\ 1\ 2\} <1\ 1\ 1>$ twin system. A schematic illustration of the $\{1\ 1\ 2\} <1\ 1\ 1>$ twinning mechanism is provided in **Fig. 7f**. Recent TEM observations have substantiated that $\{1\ 1\ 2\} <1\ 1\ 1>$ mechanical twinning is a prominent plastic deformation mechanism in the VNbTa alloy [13].

Fig. 7g demonstrates the formation of multiple parallel deformation bands within the 20% RIT samples. The presence of discernible color gradients within each band, as illustrated in **Fig. 7h**, suggests non-uniform plastic deformation within these regions. The KAM map in **Fig. 7i** reveals increased dislocation densities at the interfaces between the bands and the matrix, while lower densities are observed within the bands. Furthermore, **Fig. 7j** depicts the crystal misorientation of the bands along the path indicated by the red arrow in **Fig. 7h**. Notably, the crystal misorientation angle of these bands falls within the range of 20° – 27° , which does not correspond to the $\{1\ 1\ 2\} <1\ 1\ 1>$ (60°) and $\{3\ 3\ 2\} <1\ 1\ 3>$ (50.5°) twinning systems typically observed in BCC crystals. These findings suggest that the deformation bands are not twinning. Kink bands, which represent another type of plastic deformation in BCC metals, can enhance ductility through collaborative dislocation slip [19].

The dislocation slip results in localized lattice rotation that leads to non-unique crystal misorientation within the crystals. **Fig. 7j** demonstrates that the misorientation angles of the deformation bands range from 20° to 27° , suggesting that these bands can be classified as dislocation kink bands. The identification of kink bands can be achieved through intragranular misorientation axis (IGMA) analysis, which relies on the characterization of their characteristic Taylor axes [36]. The Taylor axis is determined by equation $T = \gamma b \times n$, where γ , b , and n represent the shear gradient, Burgers vector, and normal vector of slip

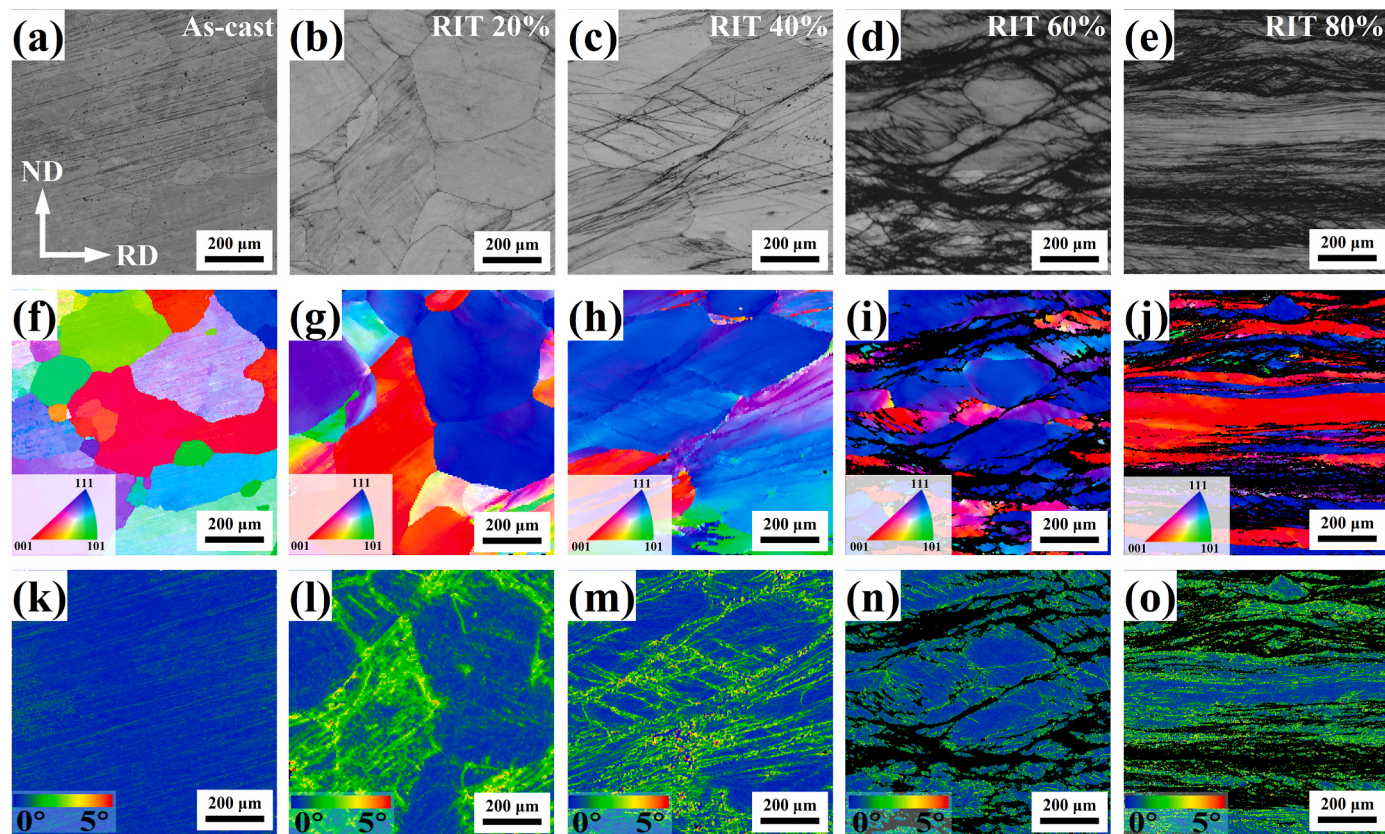


Fig. 6. (a–e) EBSD band contrast (BC) images, (f–g) inverse pole figures (IPF) and (k–o) kernel average misorientation (KAM) maps of the VNbTaTi alloy under various rolling conditions: the first to fifth columns refer to at-cast 20%, 40%, 60% and 80% reduction in thickness (RIT), respectively.

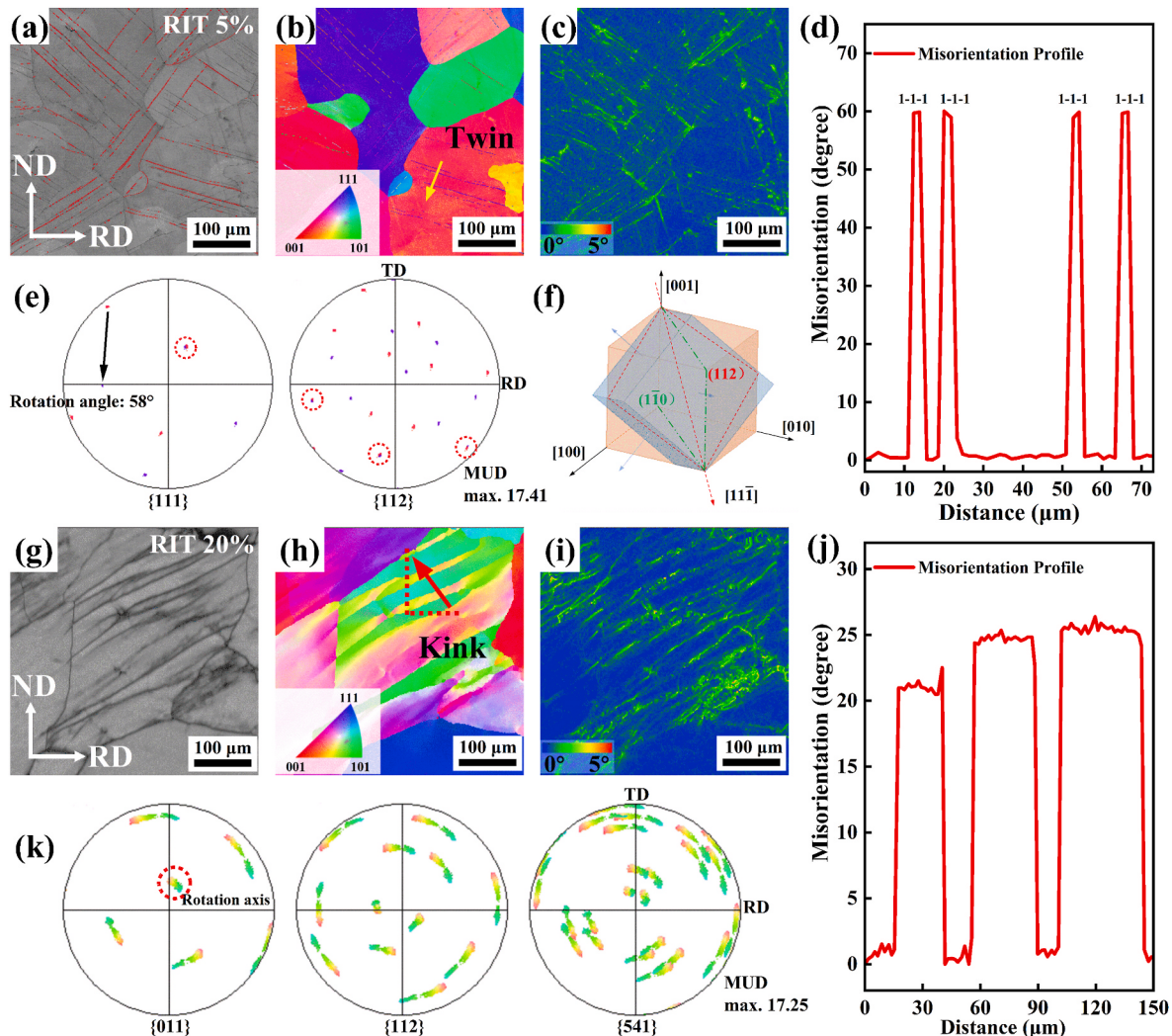


Fig. 7. EBSD images of the 5%-RIT and 20%-RIT samples of the VNbTaTi_x alloy. (a–c) The BC, IPF and KAM images of the 5%-RIT sample. (d) The misorientation profile along the arrow in (b). (e) {1 1 1} and {1 1 2} pole figures. (f) A rotating schematic of the {1 1 2}<1 1 1> twining. (g–i) The BC, IPF and KAM images of the 20%-RIT sample. (j) The misorientation profile along the arrow in (h). (k) {0 1 1}, {1 1 2} and {5 4 1} pole figures of the rectangular subsets in (h).

plane, respectively [36]. Different Taylor axes correspond to distinct dislocation slip modes in BCC crystals. For instance, the <0 1 1>, <1 1 2>, and <5 4 1> axes correspond to the {1 1 2}<1 1 1>, {1 1 0}<1 1 1>, and {1 2 3}<1 1 1> slip modes, respectively [19]. When a rotation occurs in any of the crystal planes {1 1 0}, {1 1 2}, or {5 4 1}, the resulting deformation bands can be classified as kink bands. The pole figures in Fig. 7k reveal a concentration of poles around the {0 1 1} figure, indicating that the lattice rotation axis is <0 1 1> and the {1 1 2}<1 1 1> slip system is activated.

3.4. Microstructure of the annealed alloys

Fig. 8 presents the microstructure of the annealed VNbTaTi_x alloys. The BC images in Fig. 8a–d present equiaxed grains with comparable sizes across all annealed samples. The random distribution of grain orientations (Fig. 8e–h) suggests that recrystallization is finished and deformation texture is eliminated. After the recrystallization annealing, local plastic strains have been substantially eliminated (Fig. 8i–l). The annealed alloys exhibit a uniform distribution of grain sizes, with the average size increasing from 20 μm (Ti_{0.0} alloy) to 46 μm (Ti_{1.5} alloy) (Fig. 8m–p). This observation suggests that the addition of Ti promotes grain growth during the annealing process.

3.5. Tensile properties and microhardness

The mechanical properties of VNbTaTi_x alloys were evaluated through tensile and hardness tests conducted at room temperature. Fig. 9a illustrates the typical engineering stress-strain curves obtained from tensile tests for these alloys. Initially, the alloys undergo elastic deformation, where the tensile stress increases proportionally with the strain ratio. Upon reaching the elastic limit, yielding occurs. The yield strength ($\sigma_{0.2}$) decreases from 1033 MPa (Ti_{0.0} alloy) to 691 MPa (Ti_{1.5} alloy) with increasing Ti content. The slope of the elastic σ - ϵ curves tends to decrease as the Ti content increases, indicating that the addition of Ti reduces the yield strength and elastic modulus of the alloys. Following yielding, the samples enter a stage of stable plastic deformation. The stable plastic deformation in BCC RHEAs is governed by the competition between dislocation multiplication and annihilation [37]. After undergoing significant plastic strain, the samples eventually reach a state of plastic instability, leading to crack formation and eventual fracture [37]. Fig. 9a demonstrates that all tested alloys exhibit excellent ductility, with fracture elongation (ϵ_f) exceeding 15%. Among these alloys, the Ti_{1.0} alloy displays the highest ϵ_f value of 26.9%, which surpasses that of most RHEAs. Fig. 9b reveals that the measured hardness (HV_{exp}) of the alloys decreases from 403 ± 7 HV (in the Ti_{0.0} alloy) to 300 ± 6 HV (in the Ti_{1.5} alloy) as the Ti content increases. This downward trend in

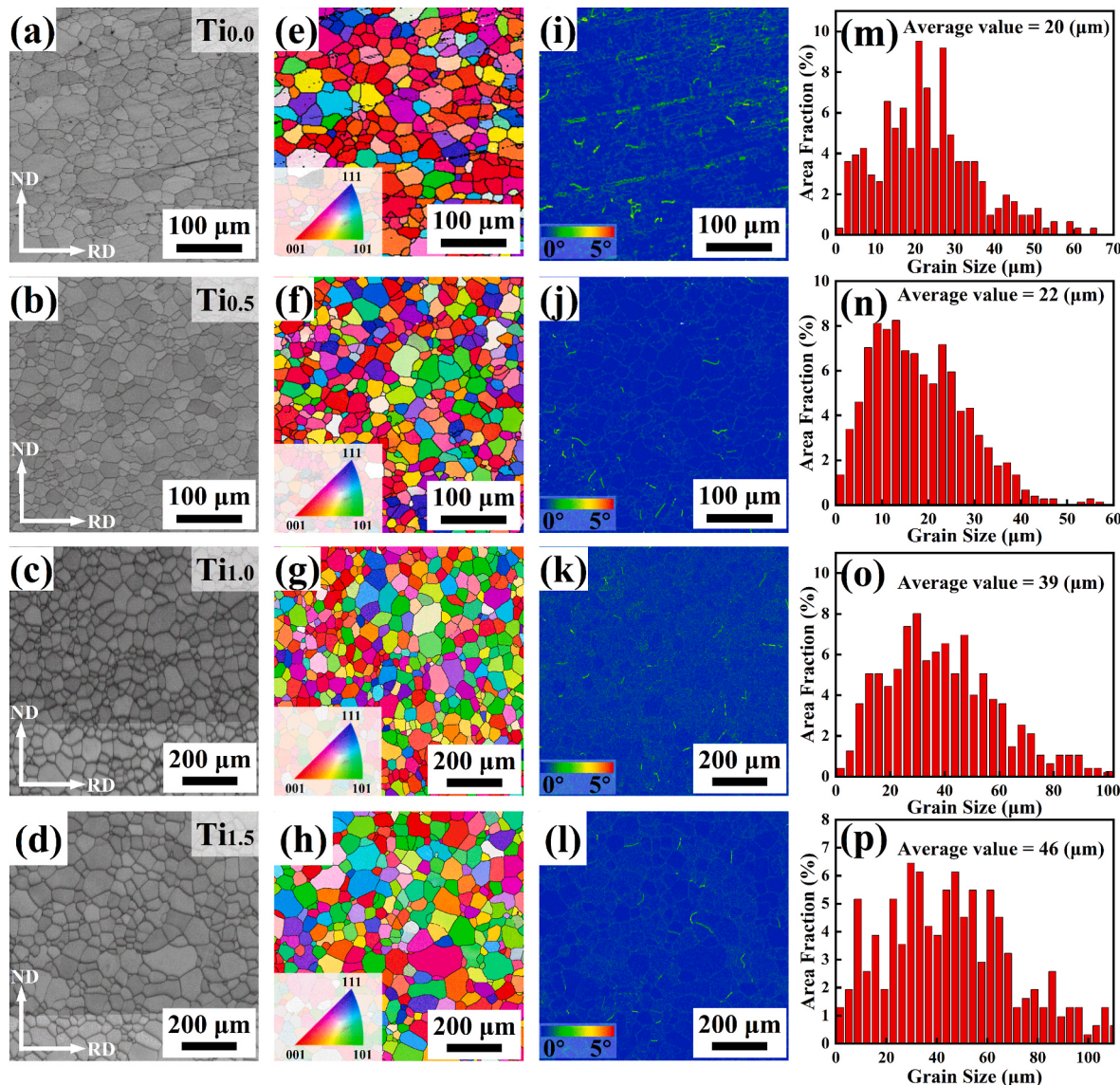


Fig. 8. (a~d) EBSD BC, (e ~ h) IPF, (i ~ l) KAM images and (m ~ p) area weighted grain size distribution of VNbTaTi_x ($x = 0.0, 0.5, 1.0, 1.5$) alloys after annealing 30 min at 1200 °C.

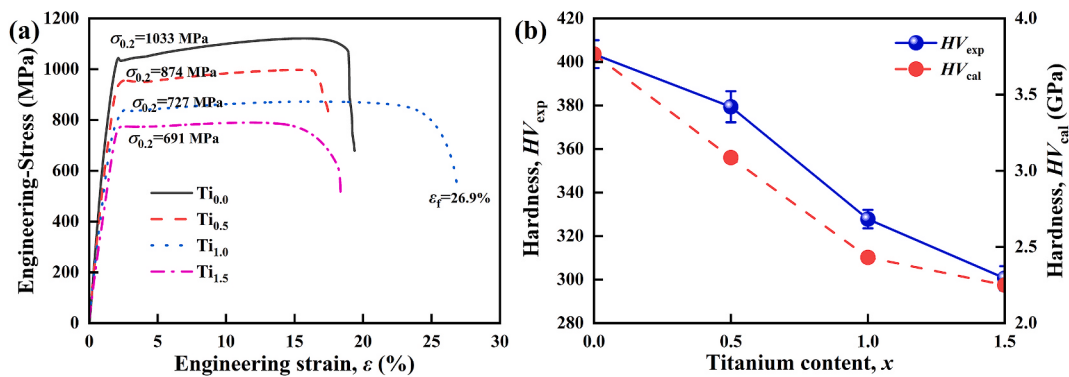


Fig. 9. (a) Tensile engineering stress-strain curves of VNbTaTi_x ($x = 0.0, 0.5, 1.0, 1.5$) alloys at room temperature; (b) Tested hardness (HV_{exp}) and calculated hardness (HV_{cal}) as a function of Ti content.

(HV_{exp}) is in good agreement with the DFT calculated hardness values (HV_{cal}).

Fig. 10 presents the macro- and micro-morphologies of the fracture

surfaces of the VNbTaTi_x alloys, providing insights into their tensile fracture behavior. The macro-morphologies (Fig. 10a-d) exhibit distinct necking and lip features, indicating the exceptional ductility of the

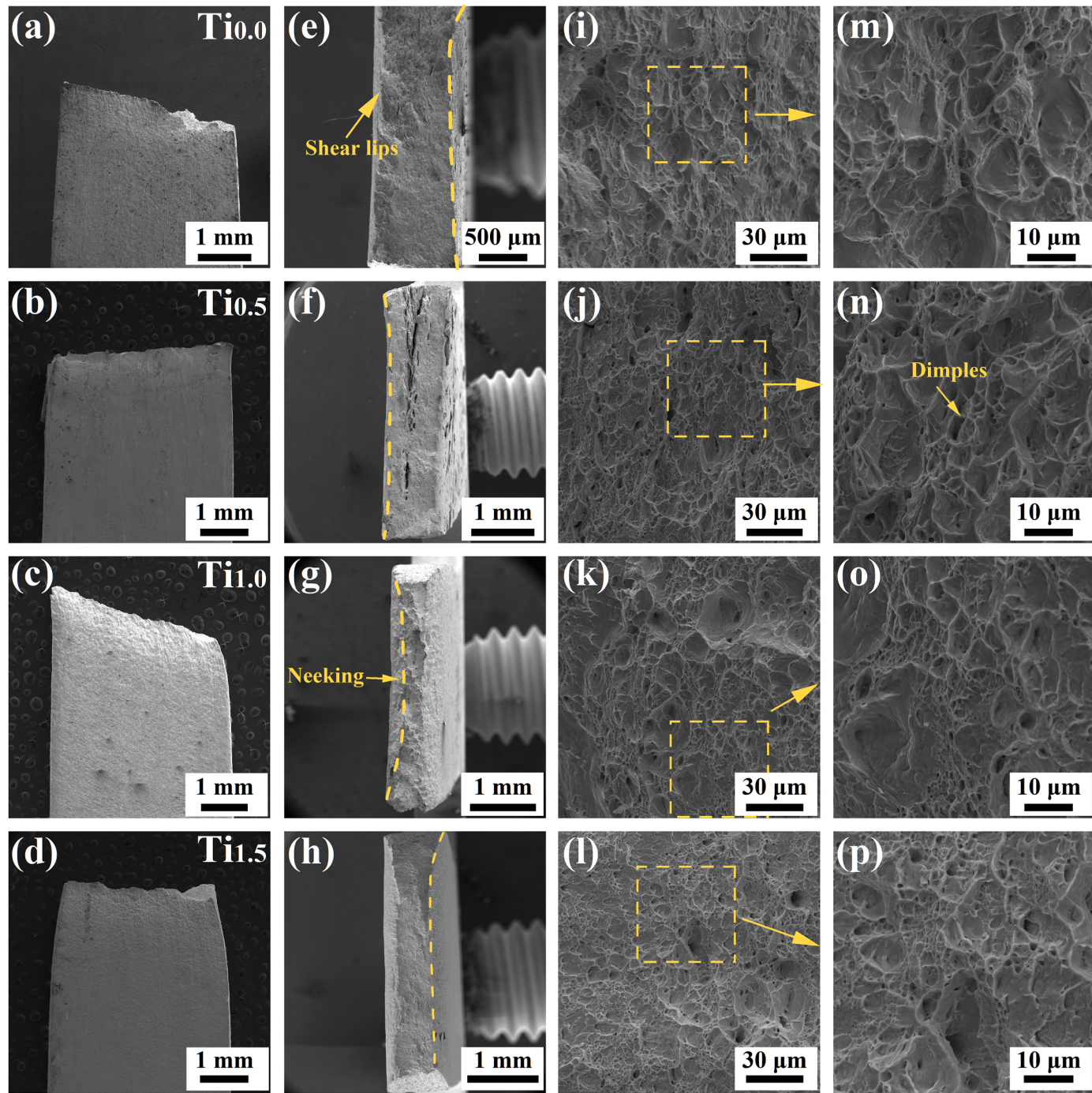


Fig. 10. The macro- and micro-morphologies of the tensile fracture surfaces of the VNbTaTi_x ($x = 0.0, 0.5, 1.0, 1.5$) alloys. The first (a-d), second (e-h), third and fourth (i-p) columns display normal-, front-, and enlarged-view morphologies of the fracture surfaces, respectively.

alloys. This observation is further supported by the analysis of the micro-morphologies (Fig. 10e–h), where numerous large and deep dimples are observed on the fracture surfaces. These findings confirm that the fracture of the VNbTaTi_x alloys is ductile.

3.6. Dislocation nucleation and twinning in MD simulations

EBSD analyses reveal that the excellent formability of VNbTaTi_x alloys at RT attributes to the activation of multiple plastic deformation mechanisms such as twinning, dislocations, and kink bonds. The precise activation mechanisms of dislocation and twinning in RHEAs are still not fully understood, despite numerous experimental investigations [14,

18,22,38]. For instance, TEM observations have revealed that the plastic deformation of RHEAs is primarily governed by the motion of $a/2<1\bar{1}1>$ -type dislocations [14,18]. To explore the potential plastic deformation mechanisms activated in the deformation of ductile BCC single-phase RHEAs, the tensile deformation of the VNbTaTi_x alloys were simulated by MD. Fig. 11a shows the MD-calculated stress-strain curves of the VNbTaTi_x alloys. As shown in Fig. 11a, the stress increases with increasing strain in the elastic stage. Upon reaching the elastic limit, yielding occurs, indicated by a rapid decline in stress with increasing strain, signifying the onset of plastic deformation. The addition of Ti results in a decrease in yield stress, consistent with the experimental findings (Fig. 9a).

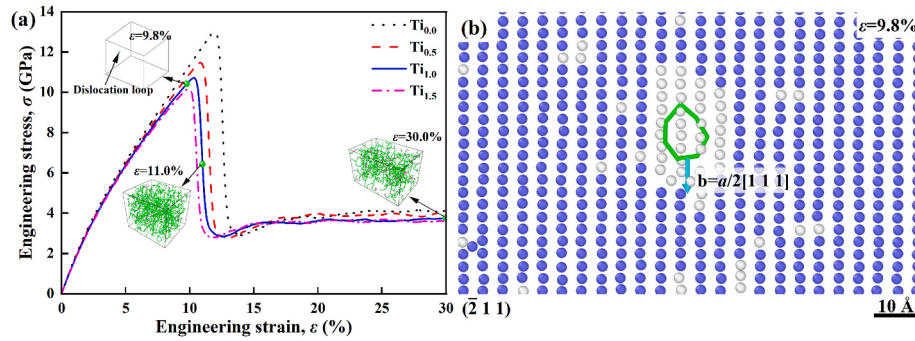


Fig. 11. (a) The MD simulated stress-strain curves of VNbTaTi_x alloys tension along the [1 1 1] direction. The insets illustrate dislocation configurations at different strains of Ti_{1.0} alloy. The green lines are $a/2<1\ 1\ 1>$ -type dislocations. (b) Atomistic configuration of the dislocation loop.

The dislocation configurations of VNbTaTi alloy at various strain ratios are shown as insets in Fig. 11a. The $a/2<1\ 1\ 1>$ -type dislocations are highlighted in green in these configurations. It can be observed that a dislocation loop nucleates within the simulation box at a strain ratio of 9.8%. Fig. 11b provides an enlarged atomistic view of the dislocation loop. Atoms with BCC structures are colored in blue, while atoms deviating from the BCC structure are marked in white. It is evident that the local deviation of atoms from the BCC lattice leads to the homogeneous nucleation of dislocations. The dislocation loop possesses a Burger vector of $a/2[1\ 1\ 1]$ and expands on the $(\bar{2}\ 1\ 1)$ crystal plane. Similar dislocation loops have been observed by TEM in other RHEAs [18]. The nucleation and expansion of dislocations result in a decrease in localized stresses within the crystal, leading to yielding and a decrease in stress, indicating the initiation of plasticity in the crystal. During the plastic deformation process, a significant number of $a/2<1\ 1\ 1>$ -type dislocations (green lines) are generated within the crystal.

Fig. 7a illustrates the occurrence of $\{1\ 1\ 2\}<1\ 1\ 1>$ deformation twin near the grain boundaries, which propagates through the grain during the initial rolling stage of the alloy. To elucidate the formation mechanism of $\{1\ 1\ 2\}<1\ 1\ 1>$ twins around grain boundaries, molecular dynamics simulations were conducted to simulate the compression of a VNbTaTi polycrystal. The compressive stress-strain curve of the VNbTaTi polycrystal is presented in Fig. 12a. The insets in Fig. 12a depict atomistic configurations of the polycrystal model at different strains. It can be observed that twin embryos form near the grain boundaries at the onset of plastic deformation ($\epsilon = 5.0\%$). Atomistic configurations in Fig. 12b–e illustrate the formation and propagation of a twin embryo. As deformation progresses, some atoms near the grain boundaries deviate from BCC lattice sites (Fig. 12b) and form partial dislocations on adjacent $(1\ \bar{1}\ 2)$ atomic layers (Fig. 12c). These partial dislocations rapidly propagate along the [1 1 1] direction, giving rise to the formation of a twin embryo. The twin embryo gradually grows as deformation increases, resulting in a stepped twin across the grain

(Fig. 12d). The angle between the twin and matrix is approximately 140° (Fig. 12e). The presence of $\{1\ 1\ 2\}<1\ 1\ 1>$ twins has also been observed in other RHEAs through TEM analysis [39]. It should be noted that more comprehensive characterizations are required in the future to gain a deeper understanding of the plastic deformation mechanisms in RHEAs, despite the confirmation of $a/2<1\ 1\ 1>$ -type dislocations and $\{1\ 1\ 2\}<1\ 1\ 1>$ twins in other RHEAs through TEM investigations [18,39].

3.7. Strengthening mechanisms

The XRD and EBSD results reveal that the as-cast and annealed samples are BCC single phase, suggesting that solid solution strength may be the major strengthening mechanisms in VNbTaTi_x alloys. The theoretical yield strength (σ_y^{cal}) can be predicated by the empirical formula [16].

$$\sigma_y^{cal} = \sigma_{mix} + \Delta\sigma_{ss} + \Delta\sigma_{gb} \quad (6)$$

where σ_{mix} , $\Delta\sigma_{ss}$ and $\Delta\sigma_{gb}$ are the contribution of pure metal mixture, solid solution strengthening and grain-boundary hardening, respectively. The σ_{mix} can be evaluated by

$$\sigma_{mix} = \sum_{i=1}^n c_i \sigma_{yi} \quad (7)$$

where c_i and σ_{yi} are the molar concentration and yield strength of the i -th elements. The contribution of solid solution strengthening is predicated by

$$\Delta\sigma_{ss} = \left(\sum_{i=1}^n \left(AG \delta_i^{4/3} c_i^{2/3} \right)^{3/2} \right)^{2/3} \quad (8)$$

where the dimensionless constant A is about 0.04; G is the shear modulus of the alloys; δ_i is the misfit parameter of the i -th element,

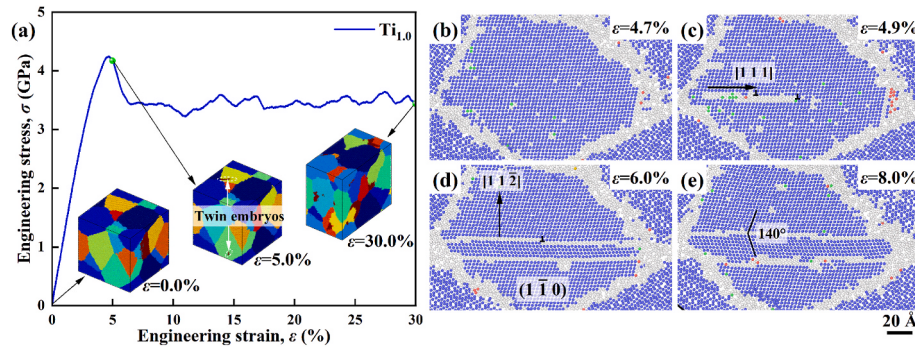


Fig. 12. (a) The MD simulated compressive stress-strain curves of VNbTaTi polycrystal including 10 nanograins about 13.7 nm in average size. The insets present atomistic configurations of VNbTaTi polycrystal at different strains. (b) Atomistic configuration of the $(1\ 1\ 2)<1\ 1\ 1>$ twinning.

$$\delta_i = \sqrt{\delta_{Gi}^2 + \beta^2 \delta_{ri}^2} \quad (9)$$

where the dimensionless constant β is about 9; the shear modulus misfit (δ_{Gi}) and atomic size misfit (δ_{ri}) of the i -th element are assessed by

$$\delta_{Gi} = \frac{9}{8} \sum c_j \delta_{Gij} \quad (10)$$

$$\delta_{ri} = \frac{9}{8} \sum c_j \delta_{rij} \quad (11)$$

where $\delta_{Gij} = 2(G_i - G_j)/(G_i + G_j)$ and $\delta_{rij} = 2(r_i - r_j)/(r_i + r_j)$; c_j is the concentration of the j -th element. The enhanced yield strength of grain-boundary hardening is predicated by [40].

$$\Delta\sigma_{gb} = \gamma G b^{1/2} d^{-1/2} \quad (12)$$

where γ is a model-dependent constant about 0.1 [41], G , b and d are the shear modulus, Burgers vector length and average grain size of the alloys, respectively. The r_i , G_i and σ_y values of elemental metals are listed in Table S1. The DFT calculated G value is about 45 GPa, 40 GPa, 35 GPa, 32 GPa for $Ti_{0.0}$, $Ti_{0.5}$, $Ti_{1.0}$, and $Ti_{1.5}$ alloys, respectively.

Fig. 13 presents the contributions of σ_{mix} , $\Delta\sigma_{ss}$ and $\Delta\sigma_{gb}$ to the yield stress of VNbTaTi_x alloys. The σ_y^{cal} value exhibits a decreasing trend as the Ti content increases, ranging from 1062 GPa ($Ti_{0.0}$ alloy) to 641 MPa ($Ti_{1.5}$ alloy). The decrease in σ_y^{cal} aligns with the experimental yield strength σ_y^{exp} , validating the effectiveness of the empirical formula in predicting yield strength. The dominant factor influencing yield strength is solid solution strengthening ($\Delta\sigma_{ss}$), as depicted in Fig. 13. The contribution of grain-boundary hardening ($\Delta\sigma_{gb}$) to yield strength is relatively limited. The addition of Ti to the alloys leads to a significant reduction in solid solution strengthening. Consequently, the simultaneous decrease in σ_{mix} , $\Delta\sigma_{ss}$ and $\Delta\sigma_{gb}$ occurs due to Ti addition, with the reduction in $\Delta\sigma_{ss}$ being the most prominent.

3.8. Lattice distortion and electronic properties

Lattice distortion is a prominent structural characteristic of high-entropy alloys and exerts a pivotal influence on their structural stability and solid solution strengthening. The non-uniform stress field generated by lattice distortion induces dislocation line bending, thereby increasing the resistance to dislocation motion and enhancing solid solution strengthening effect [22]. Fig. 14 shows that various elements randomly occupy the BCC lattice sites and exhibit obvious lattice

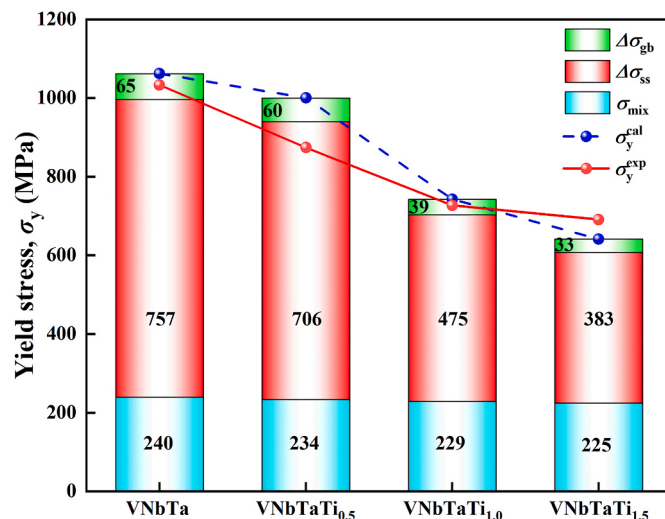


Fig. 13. Comparison of calculated yield strength and experimental results of VNbTaTi_x alloys.

distortions. The bond lengths (e.g., b_1 , b_2 , b_3) and angles (α , β) deviate from the standard bond length ($b = \sqrt{3}a/2$) and angles ($\alpha = 70.529^\circ$ and $\beta = 109.471^\circ$) of a perfect BCC lattice. The lattice distortion stems from the differences in atomic size and electronic structure among different elements [42]. It should be noted that further comprehensive investigations are required to gain a deeper understanding of the lattice distortion-induced solid solution strengthening effect in VNbTaTi_x alloys.

In order to illustrate the impact of Ti addition on the electronic structure of the alloys, the electron localization function (*ELF*) distribution on the (1 0 0) planes of the alloys is presented in Fig. 14. It can be observed that the local lattice distortion is correlated with the asymmetric distribution of electrons within the crystal. The *ELF* is a parameter commonly used to characterize the likelihood of other electrons presence in the vicinity of an electron, providing insights into electronic localization properties [43]. An *ELF* = 0 indicates complete electron delocalization, implying a low probability of electron occupation. An *ELF* = 0.5 signifies a uniform distribution of electron gas. Conversely, the value of *ELF* closes to 1 indicates a highly localized electron distribution, where electrons are trapped to form stronger covalent or ionic bonds [44]. Fig. 14a reveals that the *ELF* values are higher near the atoms, indicating electronic localization around the atomic nuclei. In the interstitial regions, the *ELF* values are close to 0.5 (green), suggesting the presence of free electron gas and metallic conductivity [45]. The regions with low *ELF* values (<0.3) are found around the V and Ti atoms (Fig. 14b), indicating electronic delocalization in these areas. With an increase in Ti content, the areas of electronic delocalization expand (Fig. 14c and d). The enlargement of these delocalization regions reduces the overall strength of interatomic bonding, consequently leading to a decrease in the yield strength of the alloys.

In order to assess the effect of Ti content on the lattice distortion of the alloys, radial distribution function (RDF) analyses were performed on the MD relaxed atomistic configurations. Fig. 15a plots the MD simulated RDF curves of VNbTaTi_x alloys. The two peaks on each RDF curve correspond to the distance distribution of the first nearest neighbor (1NN) and the second nearest neighbor (2NN) atom pairs. As shown in Fig. 15a, the maximum height of the 1NN peak decreases with increasing Ti content, meanwhile, the width of the 1NN peak is widened. The full width at half maximum (FWHM) value increases from 0.206 Å ($Ti_{0.0}$ alloy) to 0.230 Å ($Ti_{1.5}$ alloy), signifying an increase in lattice distortion. Ti addition promotes to increase the lattice distortion of RHEAs. This conclusion is supported by previous researches [16].

In addition, lattice distortion can also be assessed by variations in bond lengths and bond angles [46]. Fig. 15b illustrates the bond length distribution of the 1NN and 2NN bonds in the DFT optimized supercells. The lengths of the 1NN and 2NN bonds normally distribute about the standard values of ideal BCC lattices, i.e., $b_{1NN} = \sqrt{3}a/2$ (dash lines) and dot lines ($b_{2NN} = a$). The deviation of band lengths from their standard values demonstrates the lattice distortion of the alloys. Fig. 15c and d presents the distributions of α and β angles in the {1 0 0} planes, respectively. It is seen that α and β angles distribute normally about their standard values (dash lines). The distribution range gradually expands with the increase of Ti content. These results suggest that the lattice distortion of VNbTaTi_x alloys tends to increase with the increase of Ti content.

4. Conclusion

In this study, a series of VNbTaTi_x alloys were designed to systematically investigate the influence of Ti content on the structural and mechanical properties of RHEAs. The alloys were prepared through vacuum arc melting and solidified into dendritic BCC single-phase solid solutions. The addition of Ti leads to a reduction in mass density, yield strength, and hardness, while promoting local lattice distortion. Remarkably, all VNbTaTi_x alloys exhibit exceptional tensile ductility

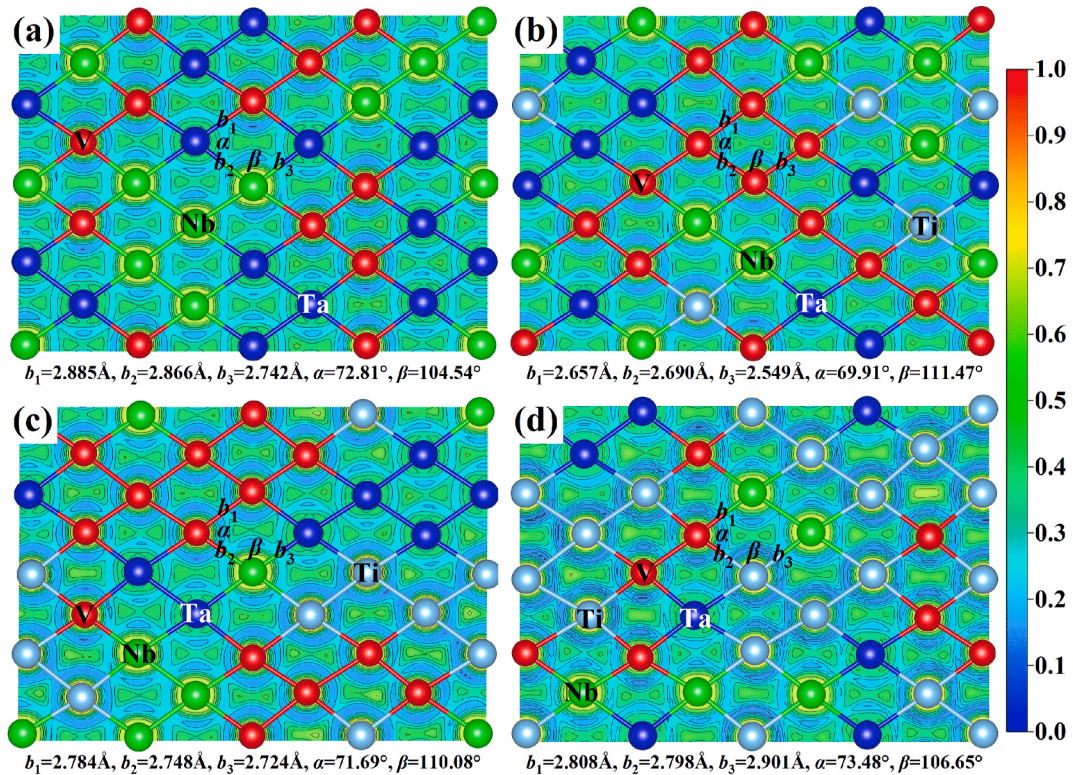


Fig. 14. Calculated electron localization function (ELF) distribution on a (1 0 0) plane of (a) $\text{Ti}_{0.0}$, (b) $\text{Ti}_{0.5}$, (c) $\text{Ti}_{1.0}$ and (d) $\text{Ti}_{1.5}$ alloys. The b_1 , b_2 and b_3 are typical bond lengths of the first nearest neighbor (1NN) atom pairs. The α and β mark the acute angle and obtuse angle of the 1NN triple atoms.

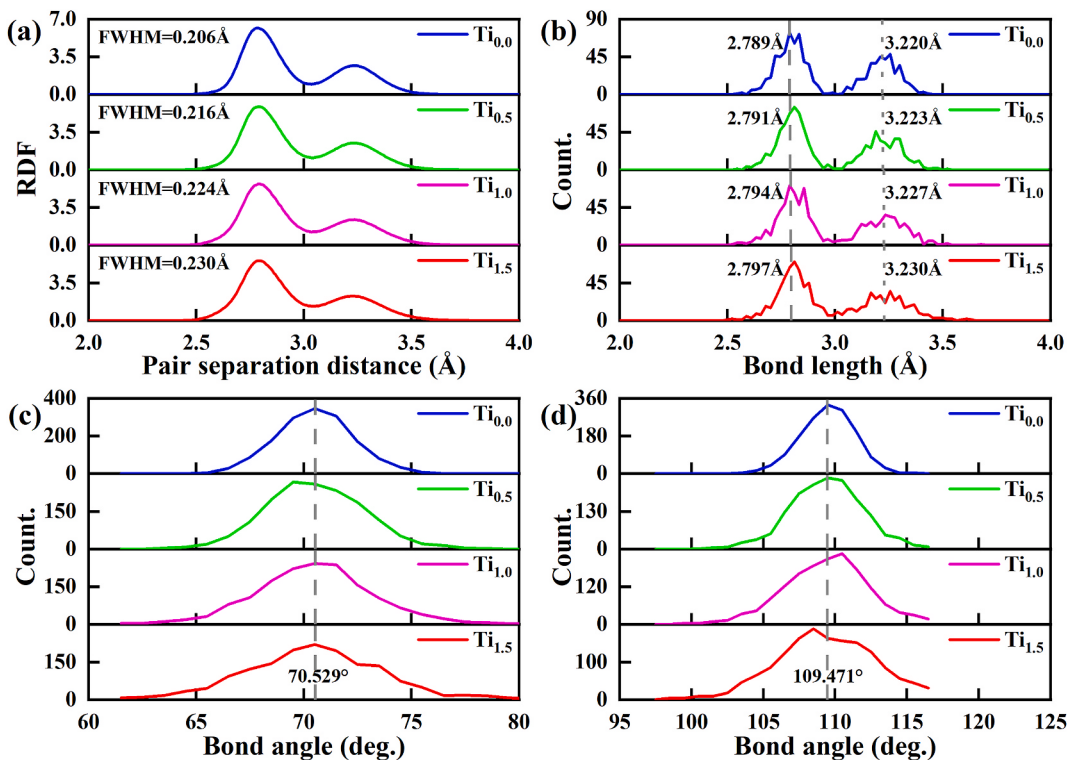


Fig. 15. (a) MD calculated radial distribution function $g(r)$ of VNbTaTix alloys. (b) DFT calculated bond length distribution of VNbTaTix alloys. (c) Acute angle (α) and (d) obtuse angle (β) distributions on the close-packed {1 1 0} planes of VNbTaTix alloys. The vertical dash lines and dot lines in (b) mark the standard bond length of the 1NN bonds ($b_{1\text{NN}} = \sqrt{3} a/2$) and 2NN bonds ($b_{2\text{NN}} = a$) of perfect BCC crystals. The vertical dash lines in (c) and (d) is the standard band angle values of the acute angles (α) and obtuse angles (β) in the {1 1 0} close-packed planes of BCC crystals.

and cold rolling formability at room temperature. The maximum tensile fracture elongation of the VNbTaTi alloy surpasses that of most RHEAs, reaching up to 26.9%. The ductility is associated with the mobility of $a/2<1\ 1>$ -type dislocations and the formation of $\{1\ 1\ 2\}<1\ 1>$ mechanical twins. However, further TEM experiments are required to comprehensively investigate the plastic deformation mechanisms, including dislocation cross-slip and interactions. Moreover, the subsequent work will systematically discuss the beneficial effects of Ti addition on enhancing the oxidation and corrosion resistance of the alloys. This study not only designs new VNbTaTi_x single-phase alloys with excellent ambient ductility but also elucidates the influence of Ti content on phase stability, lattice distortion, and mechanical properties, providing valuable insights for the design of new ductile RHEAs.

Declaration of competing interest

The authors declare that they have no known competing financial interests or personal relationships that could have appeared to influence the work reported in this paper.

Acknowledgements

This work is supported by Yunnan Science and Technology Projects (Nos. 202201AT070161, 202203ZA080001, 202302AB080023, 202303AA080015, 202301BC070001-001 and 202205AF150020); Scientific and Technological Project of Yunnan Precious Metals Laboratory (Nos. YPML-2023050205, YPML-2023050254); Yunnan High-level Talents Introduction Projects (C619300A023); L. Yang was partially supported by the postgraduate research opportunities program of HZWTECH-PROP projects.

Appendix A. Supplementary data

Supplementary data to this article can be found online at <https://doi.org/10.1016/j.jmrt.2024.04.091>.

References

- [1] Senkov ON, Gorsse S, Miracle DB. High temperature strength of refractory complex concentrated alloys. *Acta Mater* 2019;175:394–405.
- [2] Chen J, Zhou X, Wang W, Liu B, Lv Y, Yang W, Xu D, Liu Y. A review on fundamental of high entropy alloys with promising high-temperature properties. *J Alloys Compd* 2018;760:15–30.
- [3] Senkov ON, Wilks GB, Scott JM, Miracle DB. Mechanical properties of Nb₂₅Mo₂₅Ta₂₅W₂₅ and V₂₀Nb₂₀Mo₂₀Ta₂₀W₂₀ refractory high entropy alloys. *Intermetallics* 2011;19:698–706.
- [4] Feng R, Feng B, Gao MC, Zhang C, Neufeind JC, Poplawsky JD, Ren Y, An K, Widom M, Liaw PK. Superior high-temperature strength in a supersaturated refractory high-entropy alloy. *Adv. Mater.* 2021;33:e2102401.
- [5] Senkov ON, Scott JM, Senkova SV, Miracle DB, Woodward CF. Microstructure and room temperature properties of a high-entropy TaNbHfZrTi alloy. *J Alloys Compd* 2011;509:6043–8.
- [6] Li W, Xiong K, Yang L, Zhang S, He J, Wang Y, Mao Y. An ambient ductile TiHfVNbTa refractory high-entropy alloy: cold rolling, mechanical properties, lattice distortion, and first-principles prediction. *Mater. Sci. Eng. A* 2022;856:144046.
- [7] Wei S, Kim SJ, Kang J, Zhang Y, Zhang Y, Furuhara T, Park ES, Tasan CC. Natural-mixing guided design of refractory high-entropy alloys with as-cast tensile ductility. *Nat Mater* 2020;19:1175–81.
- [8] Abubaker Khan M, Wang T-L, Feng C, Sun H, Wang B, Hamza M, yasin G, Afifi MA, Liao W-B. A superb mechanical behavior of newly developed lightweight and ductile Al0.5Ti2Nb1Zr1Wx refractory high entropy alloy via nano-precipitates and dislocations induced-deformation. *Mater Des* 2022;222:111034.
- [9] Li Y, Liao W-B, Chen H, Brechtl J, Song W, Yin W, He Z, Liaw PK, Zhang Y. A low-density high-entropy dual-phase alloy with hierarchical structure and exceptional specific yield strength. *Sci China Mater* 2022;66:780–92.
- [10] Khan MA, Hamza M, Brechtl J, Nazir Z, Qaisrani NA, Yasin G, Ahmad T, Liao W-B, Liaw PK, Afifi MA. Development and characterization of a low-density TiNbZrAlTa refractory high entropy alloy with enhanced compressive strength and plasticity. *Mater Char* 2023;205:113301.
- [11] Zhang C, Wang H, Wang X, Tang YT, Yu Q, Zhu C, Xu M, Zhao S, Kou R, Wang X, MacDonald BE, Reed RC, Vecchio KS, Cao P, Rupert TJ, Lavernia EJ. Strong and ductile refractory high-entropy alloys with super formability. *Acta Mater* 2023;245:118602.
- [12] Yang L, Xiong K, Dai H, Wu H, Zhang S, Wang Y, He J, Mao Y. An ambient ductile VNbTa refractory medium-entropy alloy with super rolling formability. *Mater. Sci. Eng. A* 2024;889:145841.
- [13] Han Z, Yang G, Yang J, Tian Y, Cui J, Tian A, Liu G, Wei R, Zhang G. Superior cryogenic strength and ductility in VNbTa body-centered cubic medium-entropy alloys. *Mater Char* 2023;204:113247.
- [14] Wang L, Ding J, Chen S, Jin K, Zhang Q, Cui J, Wang B, Chen B, Li T, Ren Y, Zheng S, Ming K, Lu W, Hou J, Sha G, Liang J, Wang L, Xue Y, Ma E. Tailoring planar slip to achieve pure metal-like ductility in body-centred-cubic multi-principal element alloys. *Nat Mater* 2023;22:950–7.
- [15] Han ZD, Luan HW, Liu X, Chen N, Li XY, Shao Y, Yao KF. Microstructures and mechanical properties of Ti_xNbMoTaW refractory high-entropy alloys. *Mater. Sci. Eng. A* 2018;712:380–5.
- [16] Sun Z, Xiong K, Jin C, Zhang S, Guo L, Wu H, He J, Wu L, Wang K, Wang Y, Mao Y. An experimental and computational design low-modulus (HfNbTa)_{1-x}Ti_x multiprinciple elemental alloys with super formability for biomedical applications. *Mater. Sci. Eng. A* 2023;876:145137.
- [17] Liao H, Wu M, Deng D, Zhong W, Xiong B, Tong Y. Effects of Ti content on the microstructure, mechanical properties and corrosion behavior of Ti_xZrNb alloys. *J Mater Res Technol* 2022;19:1433–43.
- [18] Couzinié JP, Liljensten L, Champion Y, Dirras G, Perrière L, Guillot I. On the room temperature deformation mechanisms of a TiZrHfNbTa refractory high-entropy alloy. *Mater. Sci. Eng. A* 2015;645:255–63.
- [19] Raturi A, Chawake N, Biswas K, Gurao NP. Heterogeneous microstructure in nonequiatomic MoNbTaVW refractory high entropy alloy after high pressure torsion: evolution mechanisms and mechanical properties. *Mater. Sci. Eng. A* 2023;864:144530.
- [20] Zhao S, Yin S, Liang X, Cao F, Yu Q, Zhang R, Dai L, Ruestes CJ, Ritchie RO, Minor AM. Deformation and failure of the CrCoNi medium-entropy alloy subjected to extreme shock loading. vol. 9; 2023eadf8602.
- [21] Li T, Jiao W, Miao J, Lu Y, Guo E, Wang T, Li T, Liaw PK. A novel ZrNbMoTaW refractory high-entropy alloy with in-situ forming heterogeneous structure. *Mater. Sci. Eng. A* 2021;827:142061.
- [22] Wang F, Balbus Glenn H, Xu S, Su Y, Shin J, Rottmann Paul F, Knipling Keith E, Stinville J-C, Mills Leah H, Senkov Oleg N, Beyerlein Irene J, Pollock Tresa M, Gianola Daniel S. Multiplicity of dislocation pathways in a refractory multiprincipal element alloy. *Science* 2020;370:95–101.
- [23] Xiong K, Gu J. Understanding pop-in phenomena in FeNi3 nanoindentation. *Intermetallics* 2015;67:111–20.
- [24] Plimpton S. Fast parallel algorithms for short-range molecular dynamics. *J Comput Phys* 1995;117:1–19.
- [25] Qiu R, Chen Y, Liao X, Lin Y, Dou Y, He X, Yang W, Hu W, Deng H. Development of a semi-empirical interatomic potential appropriate for the radiation defects in V-Ti-Ta-Nb high-entropy alloy. *J Phys Condens Matter* 2022;35:055701.
- [26] Alexander S. Visualization and analysis of atomistic simulation data with OVITO—the Open Visualization Tool. *Model Simulat Mater Sci Eng* 2010;18:015012.
- [27] van de Walle A, Tiwary P, de Jong M, Olmsted DL, Asta M, Dick A, Shin D, Wang Y, Chen LQ, Liu ZK. Efficient stochastic generation of special quasirandom structures. *Calphad* 2013;42:13–8.
- [28] Zhang SM, Xiong K, Jin CC, Sun ZP, Li W, Mao Y. First-Principles studies on mechanical, thermodynamic and electrical properties of AgAuPd medium entropy alloy. *Rare Metal Mar. Eng.* 2022;51:4533–41.
- [29] Xiong K, Wang BW, Sun ZP, Li W, Jin CC, Zhang SM, Xu SY, Guo L, Mao Y. First-principles prediction of elastic, electronic, and thermodynamic properties of high entropy carbide ceramic (TiZrNbTa)C. *Rare Met* 2022;41:1002–14.
- [30] Kresse G, Furthmüller J. Efficient iterative schemes for ab initio total-energy calculations using a plane-wave basis set. *Phys Rev B* 1996;54:11169–86.
- [31] Blöchl PE. Projector augmented-wave method. *Phys Rev B* 1994;50:17953–79.
- [32] Perdew JP, Burke K, Ernzerhof M. Generalized gradient approximation made simple. *Phys Rev Lett* 1996;77:3865–8.
- [33] Guo S, Liu CT. Phase stability in high entropy alloys: formation of solid-solution phase or amorphous phase. *Prog Nat Sci: Mater Int* 2011;21:433–46.
- [34] Yang X, Zhang Y. Prediction of high-entropy stabilized solid-solution in multi-component alloys. *Mater Chem Phys* 2012;132:233–8.
- [35] Zhang S, Xiong K, Yang R, Dai H, Wu H, He J, Wang Y, Wu L, Mao Y. Microstructure evolution in undercooled Ag-50at. %Cu hypereutectic alloy. *J Mater Res Technol* 2023;26:1584–95.
- [36] Yamasaki M, Hagihara K, Inoue S-i, Hadorn JP, Kawamura Y. Crystallographic classification of kink bands in an extruded Mg–Zn–Y alloy using intragranular misorientation axis analysis. *Acta Mater* 2013;61:2065–76.
- [37] Zhang Z, Qi Z, Xu L, Liu R, Zhang P, Zhang Z, Langdon TG. Relationship between strength and uniform elongation of metals based on an exponential hardening law. *Acta Mater* 2022;231:117866.
- [38] Lei Z, Liu X, Wu Y, Wang H, Jiang S, Wang S, Hui X, Wu Y, Gault B, Kontis P, Raabe D, Gu L, Zhang Q, Chen H, Wang H, Liu J, An K, Zeng Q, Nieh TG, Lu Z. Enhanced strength and ductility in a high-entropy alloy via ordered oxygen complexes. *Nature* 2018;563:546–50.
- [39] Zhang X, Wang W, Wu J, Wang S, Sun J, Chung JY, Pennycook SJ. Deformation twinning in Ti48.9Zr32.0Nb12.6Ta6.5 medium entropy alloy. *Mater. Sci. Eng. A* 2021;809:140931.
- [40] Ren S, Li L, Fang Q, Li J. Modeling and analysis of yielding and strain hardening in metastable high-entropy alloys. *Phys Status Solidi* 2021;258:2100247.
- [41] Cordero ZC, Knight BE, Schuh CA. Six decades of the Hall-Petch effect—a survey of grain-size strengthening studies on pure metals. *Int Mater Rev* 2016;61:495–512.

- [42] Xiong K, Yang L, Wang F, Zhang S, You L, Wu H, Mao Y. A first-principles study the effects of nitrogen on the lattice distortion, mechanical, and electronic properties of $(\text{ZrHfNbTa})\text{C}_{1-x}\text{N}_x$ high entropy carbonitrides. *J Alloys Compd* 2023;930:167378.
- [43] Silvi B, Savin A. Classification of chemical bonds based on topological analysis of electron localization functions. *Nature* 1994;371:683–6.
- [44] Xiong K, You L, Zhang S, Yang L, Jin C, Guo L, Wang Y, Mao Y. Pressure and temperature effects on $(\text{TzrTa})\text{C}$ medium-entropy carbide from first-principles. *J Mater Res Technol* 2023;23:2288–300.
- [45] Jin C, Xiong K, Guo L, Sun Z, Li W, Zhang S, Wang Y, Mao Y. A DFT insight into the mechanical, electronic and thermodynamic properties of $(\text{TiZrHf})\text{C}$ medium-entropy carbide ceramic. *Results Phys* 2022;35:105341.
- [46] Jin C, Xiong K, Li W, Wu H, Dai H, Guo F, Luo R, Mao Y, Wang Y. Effects of V on the microstructure and mechanical properties of HfNbTaTiVx refractory multi-principle element alloys: a combined experimental and computational study. *Mater. Sci. Eng. A* 2024;898:146401.